PHYSICAL REVIEW B **77**, 054406 (2008)

Structural, electronic, and magnetic properties of tetragonal $Mn_{3-x}Ga$: Experiments and first-principles calculations

Jürgen Winterlik, Benjamin Balke, Gerhard H. Fecher, and Claudia Felser[*]
Institut für Anorganische und Analytische Chemie, Johannes Gutenberg-Universität, 55099 Mainz, Germany

Maria C. M. Alves, Fabiano Bernardi, and Jonder Morais
Instituto de Fisica e Instituto de Quimica, Universidade Federal do Rio Grande do Sul, Porto Alegre 91501-970, Brazil

(Received 10 September 2007; revised manuscript received 22 December 2007; published 6 February 2008)

This work reports on the electronic, magnetic, and structural properties of the binary intermetallic compounds $Mn_{3-x}Ga$. The tetragonal DO_{22} phase of the $Mn_{3-x}Ga$ series, with x varying from 0 to 1.0 in steps of $x=0.1$, was successfully synthesized and investigated. It was found that all these materials are hard magnetic, with energy products ranging from 10.1 kJ m^{-3} for low Mn content ($x \rightarrow 1$) to 61.6 kJ m^{-3} for high Mn content ($x \rightarrow 0$). With decreasing Mn content, the average saturation magnetization per atom increases from $0.26\mu_B$ for Mn_3Ga to $0.47\mu_B$ for Mn_2Ga. The increase in the saturation magnetization as the Mn content is reduced indicates a ferrimagnetic order with partially compensating moments of the two different Mn atoms on the two crystallographically different sites of the DO_{22} structure. This type of magnetic order is supported by *ab initio* calculations of the electronic structure that predict a nearly half-metallic ferrimagnet with the highest spin polarization of 88% at the Fermi energy for Mn_3Ga. The Curie temperature of the compounds is restricted to approximately 770 K because of a structural phase transition to the hexagonal DO_{19} phase. Thermal irreversibilities between zero-field-cooled and field-cooled measurements suggest that the $Mn_{3-x}Ga$ series belongs to the class of magnetically frustrated ferrimagnets. The most pronounced magnetic anomaly is found for Mn_3Ga.

DOI: 10.1103/PhysRevB.77.054406 PACS number(s): 61.82.Bg, 75.20.En, 75.30.Cr, 75.50.Gg

I. INTRODUCTION

Several binary alloys Mn_3Z are known that contain manganese together with a main group element Z. Those compounds exhibit various different structures and magnetic properties. Cubic Mn_3Si shows a complicated type of antiferromagnetism and is being discussed as an antiferromagnetic half-metal.[1–3] Mn_3Ge, which crystallizes in the hexagonal structure DO_{19}, exhibits a triangular spin configuration and weak ferromagnetism.[4–7] Similar magnetic properties were reported for Mn_3Sn,[8,9] which belongs to the same hexagonal structure type as Mn_3Ge. Another compound from this materials class is Mn_3Sb. This compound belongs to the cubic Cu_3Au structure type ($L1_2$) and shows weak ferromagnetism.[10,11]

Reducing the Mn content in such binary compounds, the compounds Mn_2Z are found. Mn_2Ge crystallizes in a hexagonal Ni_2In-type structure[12] and has not been investigated experimentally until now. Band structure calculations using the density functional theory led to the prediction of an antiferromagnetic ground state for Mn_2Ge.[13] Ferrimagnetic Mn_2Sb belongs to the tetragonal Cu_2Sb structure type, which is known as having a rich variety of magnetic structures.[14,15]

The present work focuses on the binary compound Mn_3Ga, which has long been an issue of interest because of its manifoldness regarding multiple structures and temperature-induced phase transitions. After some preliminary work on the binary Mn-Ga system,[16,17] Meißner and Schubert, in a comprehensive publication, established the framework for a phase diagram of this system.[18] Under suitable preparation conditions, three different phases are obtainable for the 3:1 composition of Mn and Ga. As-cast samples, obtained from repeated arc melting, crystallize in a disordered Heusler-type DO_3 phase, which was predicted by Wurmehl *et al.* to show half-metallic completely compensated ferrimagnetic behavior.[19] However, experiments provided evidence that the cubic phase of Mn_3Ga is not stable and cannot be produced without a high degree of disorder. Annealing of Mn_3Ga at high temperatures yields the hexagonal DO_{19} phase. A Mn-Ga composition with a Mn content of 71.25% was synthesized in the hexagonal phase in 1970 by Kren and Kadar.[20] This sample was investigated using neutron diffraction. Upon annealing this triangular antiferromagnetic structure at 750 K, a tetragonal DO_{22} phase was observed. This phase, which is the subject of this paper, is obtained by moderate annealing at a maximum temperature of 673 K. The phase is ferrimagnetic with magnetic moments of $-2.8\mu_B$ for Mn_I and $1.6\mu_B$ for Mn_{II} (see Fig. 1). Niida *et al.*[21] investigated several $Mn_{3-x}Ga$ compositions, but obtained single phase DO_{22}-type samples only in the range of $x=0.15-1.16$. From *ab initio* electronic structure calculations, Kübler proposed a Curie temperature of $T_C=762$ K for Mn_3Ga in the tetragonal DO_{22} structure.[22] The DO_{22} structure can be found by applying a tetragonal distortion to the DO_3 structure; therefore, Mn_3Ga can be viewed as being a tetragonally distorted, binary Heusler compound and should exhibit properties that are associated with such a compound. Because of this, Balke *et al.*[23] recently suggested the applicability of Mn_3Ga in magnetoelectronic devices and, particularly, as a suitable material for spin torque transfer applications.

The present work reports on the electronic, magnetic, and structural properties of $Mn_{3-x}Ga$ with x varying from 0 to 1.0 in steps of $\Delta x=0.1$. The electronic and magnetic structures were calculated by *ab initio* methods. The structure was investigated using powder x-ray diffraction (XRD), extended

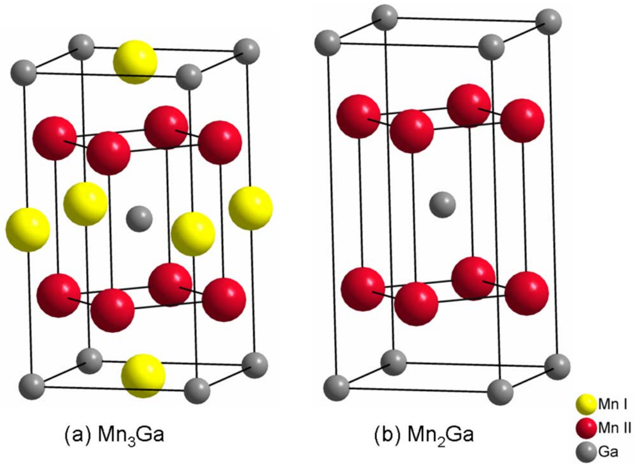

(a) Mn_3Ga (b) Mn_2Ga

FIG. 1. (Color online) Structure of tetragonal $Mn_{3-x}Ga$. Mn_3Ga (from Ref. 23) is shown in (a) and Mn_2Ga is shown in (b). The figure shows the DO_{22} crystal structure. Mn atoms (larger spheres) are represented by light (yellow) and dark (red) spheres, Ga atoms by gray spheres. In Mn_3Ga, the Mn_I atoms are located on the base quadratic faces $(1/2,1/2,0)$ and on the center plane $(0,0,1/2)$; the Mn_{II} atoms are found on the rectangular faces $(0,1/2,1/4)$, and the Ga atoms at the corners and center of the cuboid. The Mn_I atoms have a tetrahedral nearest neighbor environment. For Mn_2Ga shown in (b), only the Mn_I atoms have been removed (see model I in Sec. IV A 2); however, experiments indicate that both types of Mn atoms are removed (see text).

x-ray absorption fine structure (EXAFS) spectroscopy, and differential scanning calorimetry (DSC). The magnetic properties were studied using temperature and induction field dependent magnetometry. The transport properties of Mn_3Ga were investigated as to their dependence on temperature. The specific heats of Mn_3Ga and Mn_2Ga were investigated up to temperatures of 200 and 150 K, respectively.

II. CALCULATIONAL DETAILS

Self-consistent electronic structure calculations of the electronic and magnetic properties of Mn_3Ga and $Mn_{3-x}Ga$ were performed. The calculations were carried out using the spin polarized (SP) fully relativistic (R) Korringa-Kohn-Rostoker (KKR) method as implemented in the Munich SPRKKR program.[24,25]

The exchange-correlation functional was taken within the parametrization of Vosko, Wilk, and Nussair (VWN).[26,27] For comparison, the generalized gradient approximation (GGA) in the parametrization of Perdew *et al.*[28] was used; however, no remarkable differences were found between either parametrization. A base, $14\times14\times17$ mesh, was used for integration. The mesh corresponds to 368 (out of 3332) k points in the irreducible wedge of the Brillouin zone. The size of the muffin-tin radii was set automatically to result in space-filling spheres, and depends on the lattice parameters. f states $(l=3)$ were included in the basis of both atoms, Mn and Ga.

The properties of $Mn_{3-x}Ga$ were calculated in $I4/mmm$ symmetry using polynomial fits of a and c to the experimental lattice parameters (see Sec. IV B 1). In the DO_{22} structure type, the Mn atoms occupy two different positions. The first position (Mn_I), with multiplicity 1, is located at the Wyckoff position $2b$ $(0,0,1/2)$ and the second position (Mn_{II}), with multiplicity 2, is at $4d$ $(0,1/2,1/4)$. The Ga atom is at the Wyckoff position $2a$ (0,0,0). The lack of manganese in $Mn_{3-x}Ga$ was simulated by introducing vacancies (□) in the DO_{22} structure. To account for the random distribution of the vacancies for $x\neq0$, the calculations were carried out using the coherent potential approximation.

No essential changes of the electronic and magnetic structures of Mn_3Ga were obtained when the calculations were performed for the optimized lattice parameter as reported in Ref. 23.

III. EXPERIMENTAL DETAILS

$Mn_{3-x}Ga$ samples were prepared by repeated arc melting of stoichiometric amounts of the constituents in an argon atmosphere at 10^{-4} mbar. Care was taken to avoid oxygen contamination. The resulting polycrystalline ingots were annealed afterward at 623 K in an evacuated quartz tube for 14 days. The temperature was chosen to be safely below the structural transition temperature (see Sec. IV) and to be high enough to ensure sufficient diffusion. After annealing, the samples were quenched in an ice/water mixture so that the desired structure would be retained. This procedure resulted in samples exhibiting the DO_{22} structure (space group: $I4/mmm$) as was confirmed by using powder x-ray diffraction. The unit cell of the DO_{22} structure is displayed in Fig. 1.

DSC measurements (NETZSCH, STA 429) were performed to detect phase transitions below the melting points of the materials. The crystal structure of the $Mn_{3-x}Ga$ series was determined using XRD with excitation by Mo $K\alpha$ radiation. In addition, temperature dependent XRD was used for a detailed structural investigation of Mn_3Ga. The latter powder XRD experiments were carried out at the D10B-XPD beamline of the LNLS (Brazilian Synchrotron Light Laboratory, Campinas, Brazil).

The short range order of Mn_3Ga was investigated using EXAFS spectroscopy. The EXAFS experiments were performed at the XAFS1 beamline[29] of the LNLS using a Si(111) channel-cut monochromator. The spectra were collected at room temperature in the transmission mode at the Mn (6539 eV) and Ga (10367 eV) K edges using three ionization chambers. Ga or Mn standard foils were placed at the third chamber to check the monochromator energy calibration. The EXAFS spectra were analyzed using the IFEFFIT analysis package.[30] The isolated atom background function was removed from the experimental x-ray absorption coefficient data to yield the $\chi(k)$ signal. The Fourier transform (FT) was applied using a Hanning window with a k range of 8 Å^{-1}. The structural parameters were obtained from a least-squares fit to the data in r and k space using phase shifts and amplitudes that were obtained from the FEFF code[31] as calculated for Mn_3Ga in the DO_{22} structure and accounting for the two possible Mn sites shown in Fig. 1.

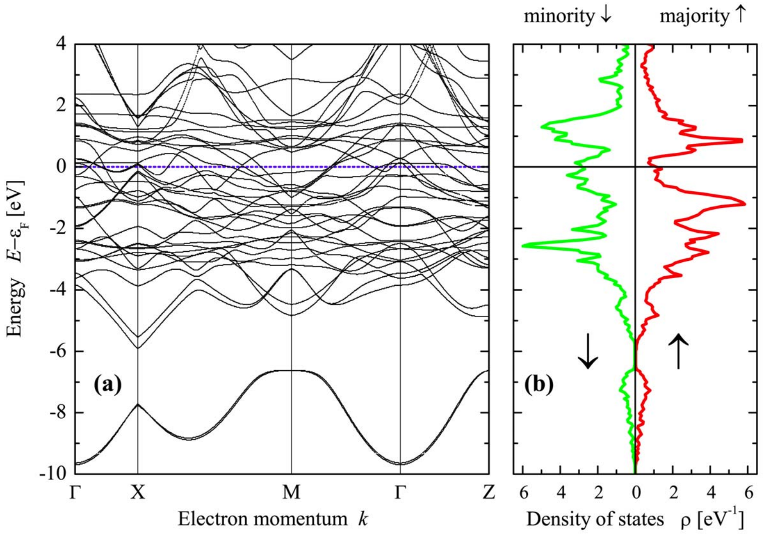

FIG. 2. (Color online) Electronic structure of Mn_3Ga. The relativistic band structure is shown in (a), along with the spin resolved density of states in (b).

The magnetic properties were investigated using a superconducting quantum interference device (SQUID, Quantum Design MPMS-XL-5) using small spherical sample pieces of approximately 5–10 mg of the sample. The transport properties and the specific heats were investigated using a physical properties measurement system (Quantum Design PPMS models 6000 and 6500, respectively).

IV. RESULTS AND DISCUSSION

A. Calculated electronic structure

1. Mn_3Ga

For the parent compound Mn_3Ga, the *ab initio* calculations indicated a ground state with ferrimagnetic order for the fully occupied DO_{22} cell. The spin magnetic moments (m_s) found from the calculations using the VWN parametrization are $-3.049\mu_B$ for Mn_I and $2.386\mu_B$ for Mn_{II}. The orbital moments are parallel to the spin moments and amount to $-0.02\mu_B$ and $0.03\mu_B$ for Mn_I and Mn_{II}, respectively. The total magnetic moment of $1.702\mu_B$ in the primitive cell is low due to the partial compensation of the moments of the Mn atoms on the two different sites. Using the GGA approach, the total magnetic moment is found to be slightly higher ($1.83\mu_B$). A particular enhancement of the orbital moments is not observed; they amount to approximately 1% of the spin moments, independent of the exchange-correlation functional used. The values for total and local moments agree well with those previously reported for full potential calculations in Ref. 23.

Figure 2 shows the full relativistic band structure and the spin resolved density of states (DOS) for Mn_3Ga. Unlike the nonrelativistic approach (see Ref. 23), the minority and majority characters of the band structure cannot be distinguished. This is only possible in the density of states. The reason is the intrinsic coupling of the spin states because of the spin-orbit interaction in the Dirac equation. The density of states, as an expectation value, can still be determined with respect to the direction of the spin. As was already discussed from the results of nonrelativistic calculations, the higher density of minority states at the Fermi energy ϵ_F (compared to the low majority density) suggests that there is a remarkable difference in the conductivity between the minority and the majority electrons as was already discussed from the result of nonrelativistic calculations.[23] Typical for a large family of compounds between transition metals and main group elements is the occurrence of a hybridization gap that splits the low lying s bands (at below approximately -7 eV) from the high lying p and d bands. The size of that gap, appearing in both spin directions, decreases with decreasing hybridization strength. This is similar to what is observed for the related Heusler compounds (see Ref. 32).

2. $Mn_{3-x}Ga$: $0<x\leq 1.0$

Basically, two different structural models were employed in the calculations for the compounds with a lack of Mn. In the first model, only the Mn_I was removed from the $2b$ position, resulting in $Mn_2(Mn_{1-x}\Box_x)Ga$ (model I). In the second model, the Mn was removed from both positions simultaneously ($4c$ and $2b$), resulting in $(Mn_{2-2x/3}\Box_{2x/3})(Mn_{1-x/3}\Box_{x/3})Ga$ (model II). The first model is based on the experimental observation (see Sec. IV C) that the magnetic moment increases as the lack of Mn increases, and is higher in Mn_2Ga than in Mn_3Ga. In the ferrimagnetic state, the moments of Mn_I and Mn_{II} are aligned in antiparallel fashion. Therefore, at least for fixed local moments, the removal of Mn_I will increase the total magnetic moment.

The calculated magnetic moments for the two structural models are compared in Fig. 3. In contrast to experimental observation, the total moment decreases slightly with increasing lack x of Mn for model II $[(Mn_{2-2x/3}\Box_{2x/3})(Mn_{1-x/3}\Box_{x/3})Ga]$. The reason is clear. Although the local moments do not stay constant, their influence is partly compensated in the total moment that is mainly given by the composition $m=(1-x/3)\ \{2m_{II}-|m_I|\}$. The behavior of the total magnetic moment in model I $[Mn_2(Mn_{1-x}\Box_x)Ga]$ follows the expected path; it increases with increasing lack of manganese. The simultaneous in-

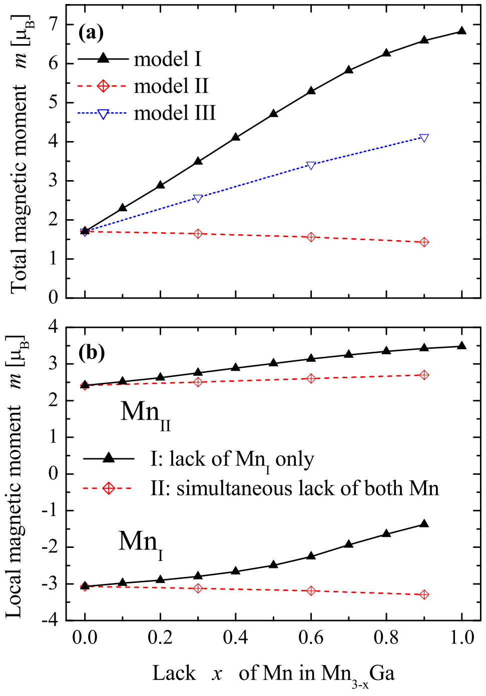

FIG. 3. (Color online) Calculated magnetic moments of $Mn_{3-x}Ga$. The total magnetic moment in the DO_{22} cell is shown in (a) and the local magnetic moments at the Mn_I and Mn_{II} sites are given in (b). Note that the magnetic moment $m=m_l+m_s$ contains both spin (m_s) and orbital (m_l) moments. See text for an explanation of the different models (I–III) used in the calculations.

crease of the moment at Mn_{II} and the decrease of the absolute value of the moment at Mn_I causes a strong increase in the overall moment.

However, the increase with x of the total magnetic moment of model I is more pronounced than that found in the experimental data. Therefore, a third model was introduced where more Mn_I is removed with increasing x than Mn_{II}. The composition in model III was chosen as $(Mn_{2-x/3}\square_{x/3})(Mn_{1-2x/3}\square_{2x/3})Ga$, which is an intermediate case between the two other models, which constitute the borderline cases of Mn removal from the crystallographic sites. For this model, twice as much Mn_I is removed as Mn_{II}. From Fig. 3(a), it is apparent that the increase of the total magnetic moment is weaker than for the $Mn_2(Mn_{1-x}\square_x)Ga$ model. Further details will be discussed later, together with the experimental data.

Figure 4 shows the DOS for the two structural models I and III, where mainly Mn_I is removed with increasing x. To cover most of the cases, the compositions with $x=0.3$, 0.6, and 0.9 were chosen for the comparisons. The VWN parametrization of the exchange-correlation functional was used in the calculations.

The general shape of the density of states is quite similar for all the cases. In particular, the minority DOS exhibits a maximum at the Fermi energy. At the same time, the majority DOS has a minimum at ϵ_F that is less pronounced at low Mn content and vanishes in the particular case of $Mn_2Mn_{0.1}Ga$. The latter result is typical for model I, where the maximum of the DOS above ϵ_F is decidedly lowered

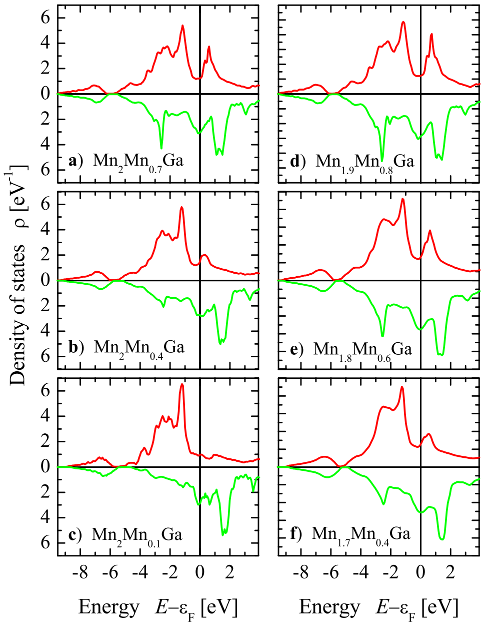

FIG. 4. (Color online) Density of states for $Mn_{3-x}Ga$. (a)–(c) show the DOS for model I: $Mn_2(Mn_{1-x}\square_x)Ga$. (d)–(f) show the DOS for model III: $(Mn_{2-x/3}\square_{x/3})(Mn_{1-2x/3}\square_{2x/3})Ga$. Shown are the selected compositions with $x=0.3$ [(a) and (d)], 0.6 [(b) and (e)], and 0.9 [(c) and (f)]. Majority densities are shown in the upper parts, and minority states in the lower parts of each of the plots.

with the removal of the Mn_I atoms. At the same time, the high density of states in the minority channel at approximately −3 eV is lowered as Mn_I atoms are removed. This explains why the localized moment of the Mn_I atom is pronouncedly reduced upon removal of those atoms from the structure. The more delocalized moment of the Mn_{II} atom is less affected. In all cases, a decrease in the size of the low lying band gap at about −6 eV that splits off the *s*-*p* states from the *d* states is observed. This indicates a weaker hybridization between Mn and Ga in the compounds with low Mn content.

B. Structural characterization

1. X-ray powder diffraction

The crystalline structure of the $Mn_{3-x}Ga$ series was examined using XRD with excitation by Mo $K\alpha$ radiation. The measurements were performed at room temperature. As examples, Fig. 5 shows the XRD results for three selected compositions ($x=0.1$, 0.5, and 1.0). The XRD data verify that, for all the compositions, the $Mn_{3-x}Ga$ samples crystallize in the Al_3Ti structure type, which belongs to the space group $I4/mmm$. The diffraction patterns for all the compositions (except for Mn_2Ga) did not show any unexpected reflexes. This indicates the phase purity of the samples. However, a small shoulder on the low angle side of the (112) reflex in the pattern for Mn_2Ga indicates an impurity, which could not be dedicated.

The lattice parameters found from a Rietveld refinement of the powder XRD data are summarized in Table I. Within

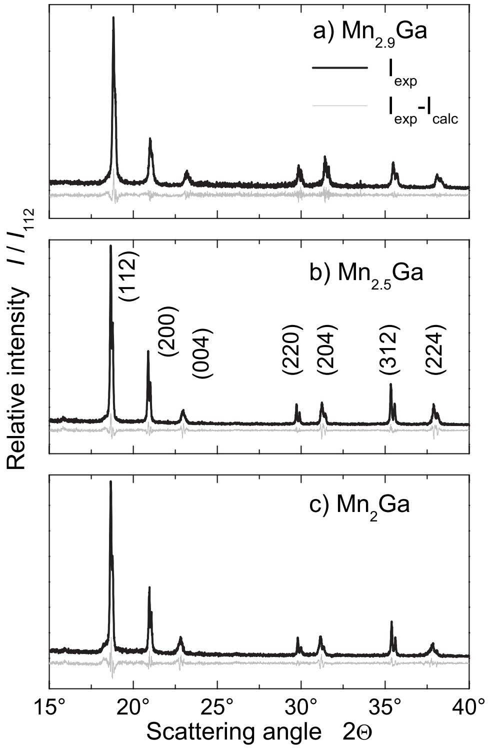

FIG. 5. Powder diffraction of $Mn_{3-x}Ga$. The measured diffractograms for $Mn_{2.9}Ga$, $Mn_{2.5}Ga$, and Mn_2Ga are compared to the curve fits from a Rietveld refinement. The spectra were excited using Mo $K\alpha$ radiation and recorded at $T=300$ K.

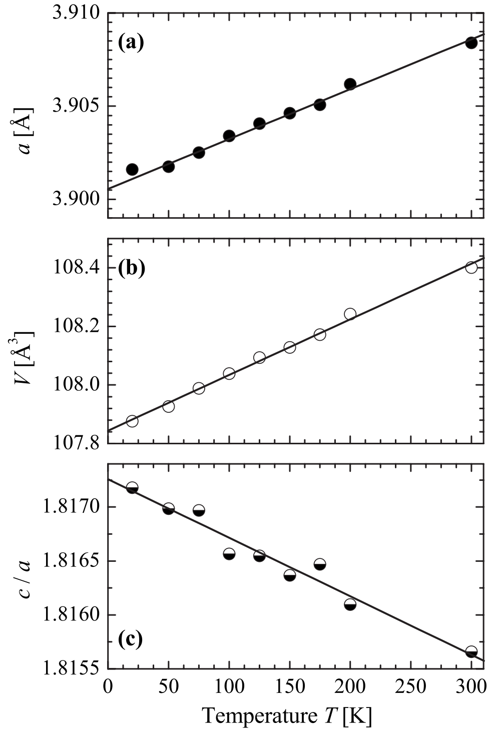

FIG. 6. Temperature dependence of the Mn_3Ga lattice parameters. The temperature dependence of the lattice parameter a and the cell volume V is shown in (a) and (b), respectively. The temperature dependence of the ratio c/a of the tetragonal lattice parameters is shown in (c).

the uncertainty of the measurements, the a parameter remains constant when the Mn content in the samples is reduced. At the same time, the c parameter increases by approximately 1.7% as x varies from 0 to 1.0. Overall, this results in an increase of the cell volume V as well as the c/a ratio with decreasing Mn content. A removal of Mn_I atoms will apparently weaken the Mn–Ga bonds along the c axis. The increase of the c parameter with x also indicates that more Mn_I atoms than Mn_{II} atoms are removed along the c axis when the Mn content is reduced. The Rietveld refinement is compatible with both of the models used for the calculations: (I) for the removal of Mn_I only as well as (III) for the removal of a higher amount of Mn_I than Mn_{II}.

TABLE I. Lattice parameter of $Mn_{3-x}Ga$. As found from a Rietveld refinement of the XRD data, the tetragonal lattice parameters a and c are tabulated for decreasing Mn content $(3-x)$. The ratio c/a and volume V are calculated from the measured values of a and c. The maximum errors for the lattice parameters are estimated from the (200) and (004) reflection peaks to be $\Delta a=0.004$ Å and $\Delta c=0.016$ Å. (Uncertainty for calculated quantities follows from error propagation.)

x	a (Å)	c (Å)	c/a	V (Å^3)
0	3.909	7.098	1.816	54.214
0.1	3.907	7.100	1.817	54.118
0.2	3.908	7.105	1.818	54.265
0.3	3.910	7.117	1.820	54.396
0.4	3.910	7.122	1.821	54.489
0.5	3.909	7.130	1.824	54.467
0.6	3.906	7.155	1.832	54.581
0.7	3.905	7.160	1.834	54.602
0.8	3.906	7.169	1.835	54.680
0.9	3.906	7.175	1.837	54.719
1	3.905	7.193	1.849	54.930

2. Temperature dependent x-ray diffraction

The crystal structure was recorded in the temperature range between 25 and 200 K using a step size of 25 K and, additionally, at 300 K using excitation by radiation with a wavelength of 1.758 66 Å. Figure 6 shows the temperature dependence of the lattice parameter a, the volume of the tetragonal unit cell V, and the c/a ratio. It is seen that the lattice parameter a and the cell volume decrease linearly with decreasing temperature. The lattice parameter c, which is not shown in Fig. 6, also exhibits a linear decrease when the temperature is reduced. However, Fig. 6(c) indicates that the c/a ratio increases when the temperature decreases. When the temperature is raised, the lattice parameter a, thus, grows stronger than the lattice parameter c. The decrease of c/a with T means that the tetragonal unit cell of Mn_3Ga becomes closer to a cubic structure as the temperature increases. However, the ratio c/a, even at room temperature, is far from the

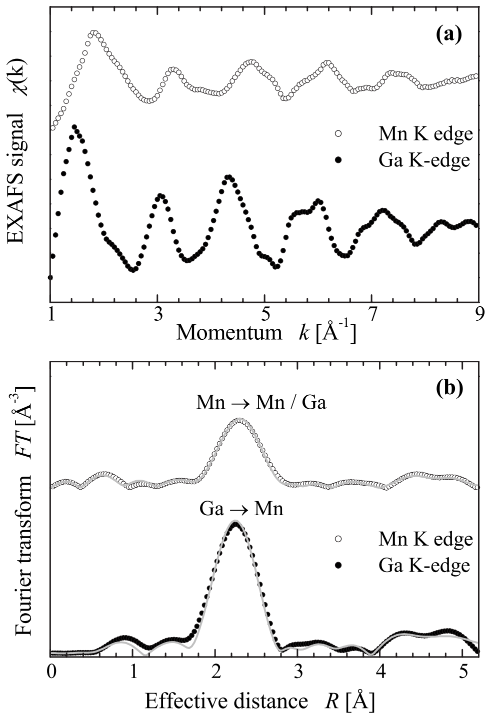

FIG. 7. EXAFS results for Mn_3Ga. EXAFS oscillations at the Mn and Ga *K* edges, extracted from the x-ray absorption spectra, are given in (a). The corresponding Fourier transforms (symbols) and best fit results (gray line) are given in (b).

ideal value ($\sqrt{2}$) that is expected for a cubic system with the DO_3 structure.

3. Extended x-ray absorption fine structure

The results from the analysis of the EXAFS measurements are summarized in Fig. 7. The EXAFS signals $[\chi(k)]$ at the Mn and Ga [Fig. 7(a)] *K* edges display the characteristic patterns for a cubic structure. The fit of the FT curves for both elements is given in Fig. 7(b). Excellent agreement between the data and theory is found as demonstrated by the low *R*-factor values (between 0.01 and 0.02). The Fourier transform at the Ga *K*-edge spectra exhibits one peak at approximately 2.2 Å and another at 4.5 Å (not corrected for the scattering phase shift) that correspond mainly to the Ga-Mn single scattering contribution in the coordination shell and the Ga-Ga contribution, respectively. Other scattering contributions appear in the quite smooth region between the two main peaks.

The FT at the Mn *K*-edge spectra exhibits peaks at similar positions, but with lower amplitudes. In fact, the Mn atoms have two possible sites: site Mn_I surrounded by 8 Mn atoms, and site Mn_{II} surrounded by (4 Mn+4 Ga) atoms. The peak at about 4.5 Å corresponds mainly to the Mn-Ga and Mn-Mn contributions. Because the coordination numbers for Ga and Mn are the same, the difference in intensity may be explained by disorder effects.

The curve fitting procedures for Mn_3Ga lead to physically reasonable numbers that are close to those provided by the theoretical structural model. The obtained values for the passive electron reduction factor (S_0^2) are about 0.7. The shift in distance (ΔR) and the Debye-Waller factor (σ^2) with respect to the theoretical model for the paths involving Ga-Ga or Ga-Mn_I(Mn_{II}) were small throughout, with $\Delta R \approx 0.04$ Å and $\sigma^2 \approx 0.007$ Å^2. For the paths involving only Mn atoms, $Mn_I(Mn_{II})$-$Mn_I(Mn_{II})$, the ΔR and σ^2 values were considerably higher, with $\Delta R \approx 0.13$ Å and $\sigma^2 \approx 0.02$ Å^2, respectively. This is in agreement with the lower amplitudes obtained at the Mn *K* edge. The curve fitting results clearly indicate the DO_{22} structure for the Mn_3Ga composition.

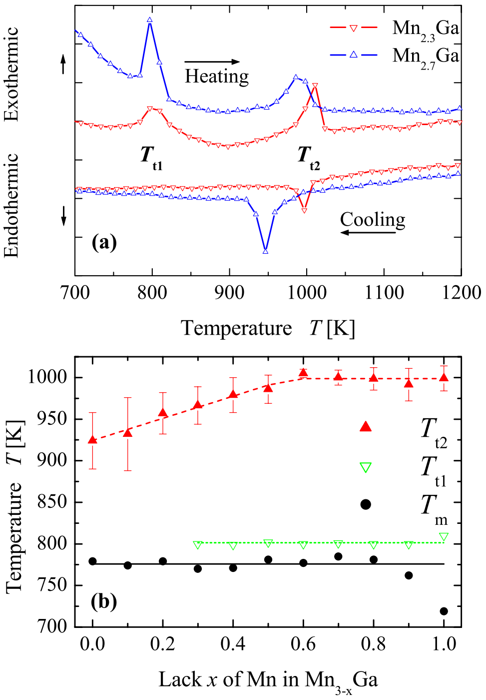

FIG. 8. (Color online) Phase transitions in $Mn_{3-x}Ga$. The plots in (a) show the results from differential scanning calorimetry for $Mn_{2.7}Ga$ and $Mn_{2.3}Ga$ in the temperature range between 700 and 1200 K upon heating of the samples, followed by cooling. The composition dependence of the phase transition temperatures is summarized in (b). T_{t1} and T_{t2} are taken from the DSC measurements, T_m is from high temperature magnetization measurements (see Sec. IV C). (Lines are drawn for clarity.)

4. Structural phase transitions

Using XRD, it was observed that the samples undergo a transition to the hexagonal DO_{19} structure at high temperatures. For this reason, DSC measurements of the entire sample series were performed to search for and investigate possible phase transitions. The DSC signals were recorded in the range from 300 to 1250 K for heating and cooling rates of 5 K min^{-1} to examine the reversibility of the occurring phase transitions. As an example, Fig. 8(a) shows two DSC curves for the compositions $Mn_{2.3}Ga$ and $Mn_{2.7}Ga$. The change of the DSC signal as a function of temperature is given. Upon heating, both substances exhibit a first maximum at a temperature T_{t1} of approximately 800 K that is not observed upon cooling, thus indicating an irreversible phase transition. In addition, a second, reversible phase transition is observed at higher temperatures, which is assigned a temperature of T_{t2}. It is seen from Fig. 8(b) that the phase transition temperature T_{t1} is independent of composition. Furthermore, it is evident that the signal at about 800 K becomes less intense and is broadened with increasing Mn content, a trend that was observed throughout the entire series. For $x \leqslant 0.2$, the determination of this phase transition at T_{t1} was impossible because the levels of the signals were too low. Nevertheless, the magnetic measurements (Sec. IV C) also indicate that there is a magnetic phase transition between 750 and 830 K in all the samples. The phase transition observed using DSC at T_{t1} corresponds to a transition to the high temperature hexagonal phase DO_{19} (structure type: Ni_3Sn, space group: $P6_3/mmc$). The structural nature of the phase transition was verified experimentally by annealing the samples at a temperature of 873 K and then examining the crystal structure using XRD.

From Fig. 8(b), it is seen that the signals at temperature T_{t2} exhibit hysteresis between heating and cooling that is due to the intrinsic effects of DSC. The shift between the extrema depends on the amount of material used as well as on the rates of temperature change. Therefore, the mean value of T_{t2} is displayed in Fig. 8(b) with error bars indicating the differences between the endothermic and exothermic values. The phase transition appears throughout the entire range of sample composition. It is clear that T_{t2} increases with decreasing Mn content and saturates for $x \geqslant 0.6$ at 1000 K. It is very likely that this corresponds to an order↔disorder transition in the hexagonal phase with preserved symmetry. Such a transition would hardly be detectable with XRD because the scattering amplitudes of Mn and Ga have similar magnitudes. It appears that this high temperature phase transition at T_{t2} changes the sample properties in such a way that the first phase transition at approximately 800 K can no longer occur upon cooling.

C. Magnetic properties

The results of the induction field dependent magnetization measurements are displayed in Fig. 9. All samples exhibit hard magnetic behavior at temperatures below the phase transitions to the hexagonal DO_{19} phase. For $Mn_{2.9}Ga$, hysteresis loops at three different temperatures are displayed in Fig. 9(a). It is seen that the magnetic moment is stable up to a temperature of 400 K.

For the compounds Mn_3Ga and $Mn_{2.9}Ga$, Table II summarizes the values of the coercitive fields H_c, remanences B_r, the specific energy products $E = H_c \times B_r$, and the energy integrals $W_H = \oint H dB$ at temperatures of 5, 300, and 400 K, respectively. The energy products E of Mn_3Ga and $Mn_{2.9}Ga$ are comparable to those of other hard magnetic materials such as Alnico 6. However, the coercitivities of Mn_3Ga and $Mn_{2.9}Ga$ are approximately four to five times higher than that of Alnico 6. The relatively low saturation magnetizations, due to the ferrimagnetic order, make the materials comparable to ferrites and related materials. From a direct integration of the magnetization loops, the energy integral $W_H = \oint H dB$ gives the hysteresis loss per cycle. For Mn_3Ga and $Mn_{2.9}Ga$, it is between three and four times larger than the energy product. For an ideal hard magnet, a nearly rectangular hysteresis loop $[B(H)]$ with $W_H \approx 4E$ and $E = BH_{max}$ is expected. The maximum energy product $BH_{max} = \max(-B \times H)$ is an energy parameter of interest for the manufacture of magnets. It represents the maximum useful magnetic energy of a permanent magnet. Its value is obtained by multiplying B and H in the second (or fourth) quadrant of the hysteresis loop. Figure 10 shows a plot of BH and the maximum energy product for the case of Mn_3Ga. The value of $BH_{max} \approx 18\ \mathrm{kJ\ m^{-3}}$, like the other energy values, is comparable to the value found in magnets from the Alnico series.

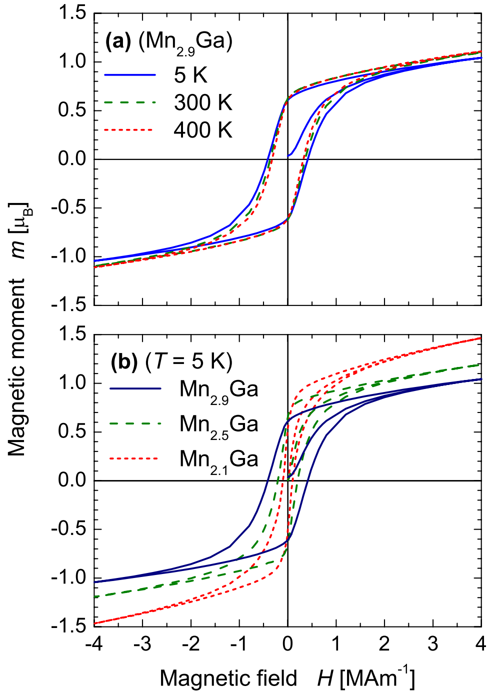

FIG. 9. (Color online) Magnetic properties of $Mn_{3-x}Ga$. The field dependent magnetization for $Mn_{2.9}Ga$ at temperatures of 5, 300, and 400 K is given in (a). Hysteresis loops for $Mn_{2.9}Ga$, $Mn_{2.5}Ga$, and $Mn_{2.1}Ga$ at $T = 5$ K are given in (b).

The hysteresis loops for $Mn_{2.9}Ga$, $Mn_{2.5}Ga$, and $Mn_{2.1}Ga$ are given in Fig. 9(b). The curves reveal a trend that is observed throughout the entire sample series. The coercitivity H_c decreases upon removal of Mn (increasing x). The remanence B_r does not strongly depend on x. Since complete saturation is not reached up to an induction field of 5 T for all samples, the value of the saturation magnetization cannot be determined. However, the maxima of the magnetic moments (at 5 T) of the series clearly increase with increasing x. This accords well with the structural properties (Table I). The increase of the lattice parameter c with increasing x, which is caused by the removal of the Mn_I atoms along the c axis, leads to a reduction of the magnetic compensation in the ferrimagnetic unit cell of Mn_3Ga. This explains why, at a given induction field, the magnetic moments increase when Mn is removed from Mn_3Ga.

Calculated and measured magnetization data are compared in Fig. 11. When going from Mn_3Ga to $Mn_{2.1}Ga$, an increase in magnetization of about 80% is found experimentally. The increase in the calculated values is much larger

TABLE II. Hard magnetic properties of Mn_3Ga and $Mn_{2.9}Ga$. Values are provided at low and elevated temperatures T of the coercitive field H_c, the remanence B_r, the specific energy product E, the energy integral W_H, and the maximum energy product BH_{max}. (Errors for the measured quantities are ΔH_c=2 kA m^{-1} and ΔB_r=0.5 mT. Errors for the calculated quantities E, W_H, and BH_{max} may be found using error propagation.)

	T (K)	B_r (T)	H_c (kA m^{-1})	E (kJ m^{-3})	W_H (kJ m^{-3})	BH_{max} (kJ m^{-3})
Mn_3Ga	5	0.136	453	61.6	203	18.3
	300	0.133	383	50.9	176	14.4
	400	0.130	342	44.5	149	12.7
$Mn_{2.9}Ga$	5	0.131	412	54.0	171	15.4
	300	0.132	359	47.4	158	13.9
	400	0.131	322	42.2	140	12.2

(≈300%) for model I, where only Mn_I is removed. According to model III, the simultaneous removal of Mn_I and Mn_{II} results in a reduced increase of 140% if it is assumed that twice as much Mn_I as Mn_{II} is removed.

Table III provides an overview of the physical properties of the $Mn_{3-x}Ga$ series. It is evident that varying the Mn content allows a simultaneous continuous tunability of coercitivity, saturation magnetization, and energy product, making the desired properties of the materials easily adjustable.

The (mass) density ρ of $Mn_{3-x}Ga$ decreases drastically by about 30% with increasing x. This is because the number of Mn atoms in the unit cell decreases while the volume of the unit cell increases with x. The decrease is, nevertheless, linear and a fit results in $\rho(x)=(1-0.2441x)7189$ kg m^{-3}. This means that the decrease of the density is governed by the loss of mass since a slope of about -0.2342 is expected for a fixed volume. The magnetic transition temperature is nearly constant with a mean value of $\overline{T_m}=(775\pm 2)$ K (omitting the value at $x=1$). The comparatively low transition temperature for Mn_2Ga may be attributed to the impurity that was found from XRD measurements (see Sec. IV B 1). From Table III, it is apparent that $Mn_{3-x}Ga$ becomes magnetically softer with decreasing Mn content. All three energy parameters E, W_H, and BH_{max} decrease with increasing x. At the same time, a decrease of the coercitivity and a maximum of the remanence at intermediate Mn concentrations are observed.

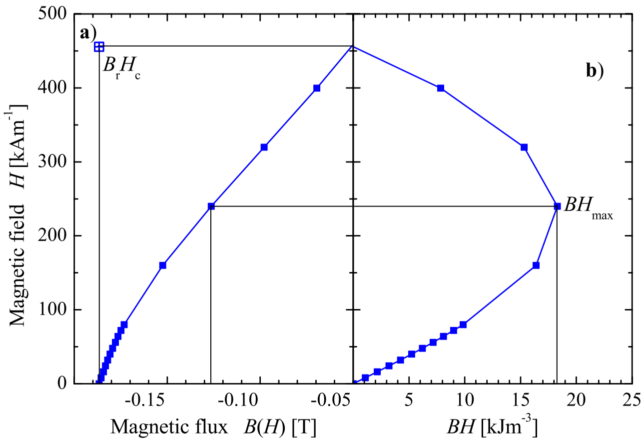

FIG. 10. (Color online) BH_{max} of Mn_3Ga. The second quadrant of the hysteresis loop $B(H)$ recorded at T=5 K is shown in (a). The calculated values for $BH(H)=-B(H)\times H$ are given in (b). The maximum value BH_{max} of approximately 18 kJ m^{-3} is found for a magnetic field of ≈250 kA m^{-1} and a flux density of ≈0.07 T. [Note that the x (H) and y (B,BH) axes are interchanged for better comparison.]

The temperature dependence of the magnetization is shown in Fig. 12 for the cases of Mn_3Ga and Mn_2Ga. In the low temperature region, the measurements were performed using induction fields of 0.1 T under zero-field-cooled (ZFC) and field-cooled (FC) conditions. For the ZFC measurements, the samples were first cooled to a temperature of 1.8 K without applying a magnetic field. After applying an induction field $\mu_0 H$, the sample magnetization was recorded as the samples were heated to the maximum temperature. Immediately afterward, the FC measurements were performed in the same field as the temperature was lowered to 1.8 K. The results for low temperatures are shown in Figs. 12(a) and 12(b). Evidently, the curves show no regular ferro-, antiferro-, or ferrimagnetic behavior. Magnetic transitions

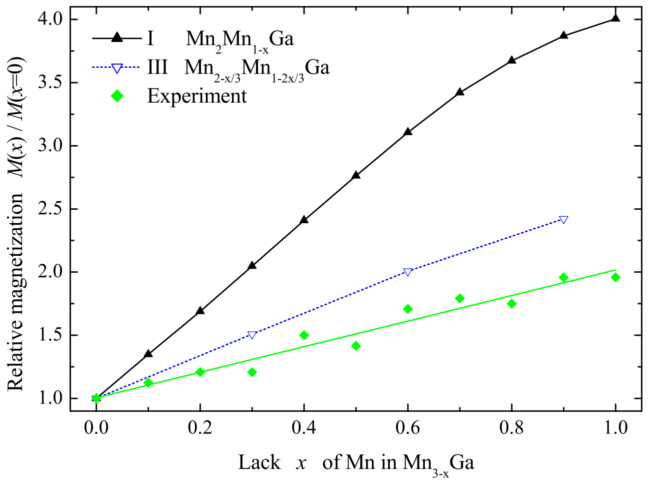

FIG. 11. (Color online) Comparison of magnetization data for $Mn_{3-x}Ga$. The values are normalized to x=0 for better comparison. Experimental values are for an induction field of 5 T. Calculated values for models I and III are seen in Sec. IV A 2.

TABLE III. Magnetic properties of $Mn_{3-x}Ga$. The following are tabulated: density ρ (at $T=300$ K), magnetic moment m per atom (at $\mu_0 H=5$ T, the high temperature magnetic transition T_m, remanence B_r, coercitive field H_c, specific energy product E, energy integral W_H, and the maximum energy product BH_{max}. The magnetic properties are given for 5 K. (Maximum errors were determined to be $\Delta m=5\times10^{-3}$ μ_B, $\Delta T_m=5$ K, $\Delta B_r=0.5$ mT, and $\Delta H_c=2$ kA m^{-1}. Other uncertainties are found from error propagation.

x	ρ (kg m^{-3})	m (μ_B)	T_m (K)	B_r (T)	H_c (kA m^{-1})	E (kJ m^{-3})	W_H (kJ m^{-3})	BH_{max} (kJ m^{-3})
0	7184	0.26	779	0.137	453	61.6	203	18.3
0.1	7028	0.27	774	0.131	412	54.0	171	15.4
0.2	6841	0.29	779	0.137	344	47.1	159	12.3
0.3	6657	0.29	770	0.130	315	41.0	146	10.4
0.4	6478	0.36	771	0.155	249	38.6	150	8.8
0.5	6313	0.34	781	0.139	205	28.5	122	6.8
0.6	6133	0.41	777	0.127	149	18.9	116	3.8
0.7	5963	0.43	785	0.125	137	17.1	114	3.4
0.8	5788	0.42	781	0.114	124	14.1	105	2.9
0.9	5617	0.47	762	0.111	100	11.1	91	2.6
1	5429	0.47	723	0.099	102	10.1	90	2.4

are observed at temperatures of 164 K for Mn_3Ga and approximately 145 K for Mn_2Ga in the ZFC measurements. These transitions exhibit thermal irreversibilities between the ZFC and the FC measurements. This type of behavior is known from spin glasses and other frustrated systems with multidegenerate ground states.[33] Thermal irreversibilities, such as the ones mentioned above, are found in all samples of the entire series. Furthermore, the irreversibilities were observed using different magnetic induction fields that ranged from 2.5 mT to 5 T. These irreversibilities led to the conclusion that the $Mn_{3-x}Ga$ series is a set of frustrated ferrimagnets.[34,35] The difference of the magnetization between ZFC and FC measurements decreases with increasing x. For Mn_3Ga, there is a difference of 131% between ZFC and FC measurements, while the same difference constitutes only 9% for the case of Mn_2Ga. Apparently, the magnetic frustration is lowered upon removal of Mn atoms from the unit cell. This also supports model III. According to model I, where only Mn_I atoms are removed in Mn_2Ga, a ferromagnetic order should remain. The remaining magnetic frustration in Mn_2Ga, thus, provides evidence that Mn_2Ga contains both Mn_I and Mn_{II} atoms with an at least partially random distribution among both crystallographic sites. For some intermediate compositions, an accurate determination of the transition temperatures was not clearly possible because the transitions were very broad or there was no distinct maximum at all (in the cases of $x=0.2$ and 0.4). The transitions that could be determined span a temperature range from 145 to 172 K. It appears, however, that there is no distinguished correlation of the transition temperatures with x, the magnetic moment, or the lattice parameters. This hints also on a partial random distribution of the voids on both Mn positions.

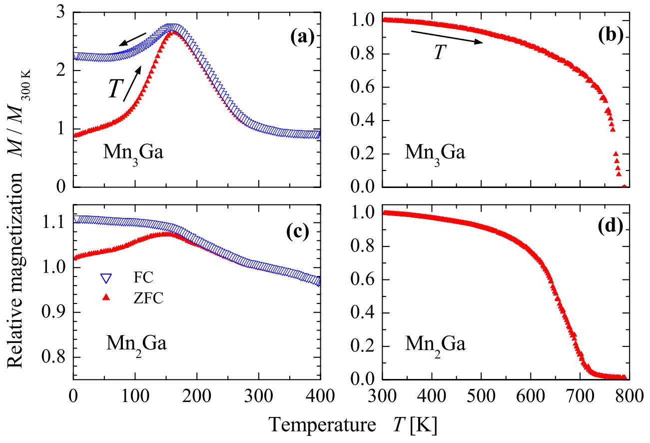

FIG. 12. (Color online) Temperature dependent magnetization of Mn_3Ga and Mn_2Ga. The temperature measurements in the range from 5 to 400 K under ZFC and FC conditions are given in (a) and (b). The high temperature measurements ($T>300$ K) upon heating of the samples are given in (c) (from Ref. 23) and (d). For better comparison, the data are normalized to the values at 300 K [note the offset of the Mn_2Ga low temperature magnetization data in (c)].

The drastic decreases of the magnetizations at $T_S \approx 780$ K for Mn_3Ga and at $T_S \approx 720$ K for Mn_2Ga, which are seen in the high temperature SQUID measurements in Figs. 12(c) and 12(d), are caused by structural transitions from the tetragonal to the hexagonal phases.[18,20] These structural phase transitions are easily detected using differential scanning calorimetry. The occurrence of the structural phase transitions makes it impossible to determine the Curie temperature of the tetragonal phase of $Mn_{3-x}Ga$. The structural phase transitions take place at temperatures below the expected magnetic phase transition. The high temperature magnetic measurements also support the results from DSC (see Sec. IV B 4). The lower temperatures of T_m compared to T_{t1} [see Fig. 8(b)] are addressed to an intrinsic effect of the DSC, where the signals depend on the heating rates; higher heating rates and larger amounts of material will apparently shift the signal to higher temperatures. The magnetic measurements also show the onset of magnetization at T_m upon cooling. This confirms the assumption that T_m and T_{t1} correspond to

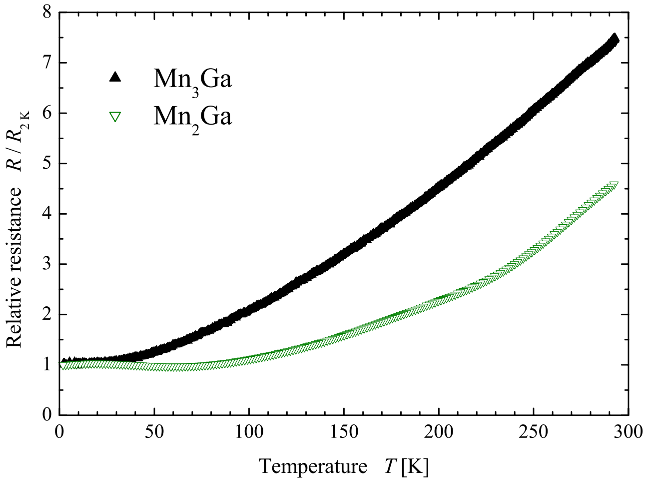

FIG. 13. (Color online) Electric resistance measurements of Mn$_3$Ga and Mn$_2$Ga. The measurements were performed upon heating of the samples. For better comparison, the data are normalized to the values at 2 K.

the magnetic transition temperature of the hexagonal DO$_{19}$ phase rather than to the Curie temperature of the tetragonal DO$_{22}$ phase. The magnetic transition and the structural transition occur nearly simultaneously. Nevertheless, this should not cause problems in designing devices using this material because it is very stable in the temperature range below 700 K and, thus, well suited for applications at and far above room temperature.

D. Transport properties

The resistance of Mn$_3$Ga and Mn$_2$Ga was measured as a function of temperature upon heating and cooling in the range from 2 to 300 K. The heating curves are shown in Fig. 13. The values are normalized to the value at 2 K for better comparison. The samples show typical metallic behavior, where the resistances increase with increasing temperature. At approximately room temperature, the resistances of Mn$_3$Ga and Mn$_2$Ga exhibit a linear slope. Only a very small thermal hysteresis was found between the heating and cooling curves and it can be attributed to the precision of the measurements. Residual resistivity ratios of approximately 8 for Mn$_3$Ga and 4.5 for Mn$_2$Ga were determined for the ratio between the 2 and 300 K measurements. For polycrystalline ingots, the comparably large value of 8 indicates the high quality of the Mn$_3$Ga samples. However, the value for Mn$_2$Ga is significantly lower. This fact is addressed to the unknown impurity which was found in the XRD measurement (Sec. IV B 1). The low temperature magnetic transitions, as mentioned in Sec. IV C, are not observable in the resistivity measurements. It is known from other frustrated systems that the transitions may be shifted to much higher temperatures (values of 150% are quite common; shifts of up to more than 1000% are known) or are simply not detectable in the resistivity measurements.[33,36–38] The latter is the most probable reason because a sharp phase transition is also not detectable in the magnetic measurements.

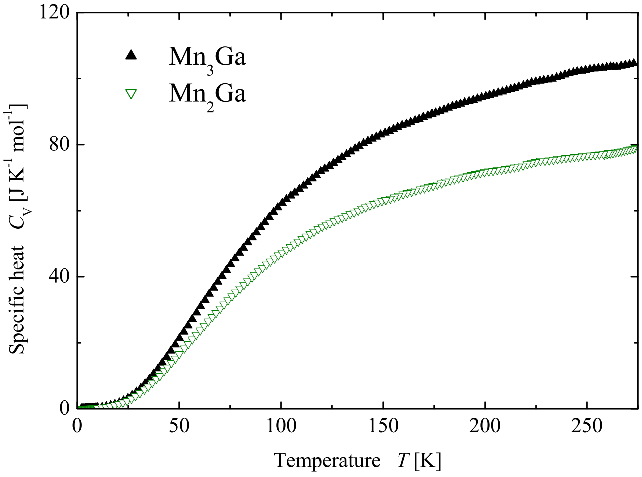

FIG. 14. (Color online) Specific heat of Mn$_3$Ga and Mn$_2$Ga. The measurements were performed upon heating of the samples.

E. Specific heat

The specific heat of Mn$_3$Ga and Mn$_2$Ga was measured as a function of temperature. The results are displayed in Fig. 14. The curves show typical metalliclike specific heat shapes composed of electronic and phononic contributions to the specific heats. To a good approximation, they follow T^3 laws below 30 K. A low temperature fit (<5 K) of the data results in electron specific heats of 19 ± 0.2 mJ/(mol K^2) and 16 ± 0.2 mJ/(mol K^2) for Mn$_3$Ga and Mn$_2$Ga, respectively. Those values are rather large compared to pure Mn [$\gamma_{\mathrm{Mn}} = 9.2$ mJ/(mol K^2)].

The magnetic anomalies, which were mentioned in Sec. IV C, are not directly visible from the specific heat curves of Mn$_3$Ga or Mn$_2$Ga. This is expected, because the magnetic anomaly covers a wide temperature range rather than appearing as a sharp transition. The situation changes when having a closer look at the derivative of C_v. Figure 15(a) compares the differentiated specific heat of Mn$_3$Ga and Mn$_2$Ga to the magnetic irreversibility at low temperatures ($T < 250$ K). The magnetic irreversibility is determined by the difference $m_{FC} - m_{ZFC}$ between the magnetization measured under FC and ZFC conditions. It is evident from Fig. 15(b) that the magnetic anomaly is more pronounced in the case of Mn$_3$Ga. For Mn$_2$Ga, the curve is flatter than what is expected from the $M(T)$ dependence shown in Fig. 12. This fact can be addressed to a lowered degree of frustration as noted in Sec. IV C. From the comparison of Figs. 15(a) and 15(b), it is obvious that the magnetic anomaly coincides with a pronounced change of the slopes of the differentiated specific heat curves. For Mn$_3$Ga, these changes of the slopes coincide with the strong changes in the magnetic irreversibility. For Mn$_2$Ga, such changes are much smaller. This is expected from the less pronounced effect that is seen in the temperature dependence of the magnetization.

V. SUMMARY

The series of compounds Mn$_{3-x}$Ga was investigated experimentally and by first-principles calculations. In summary,

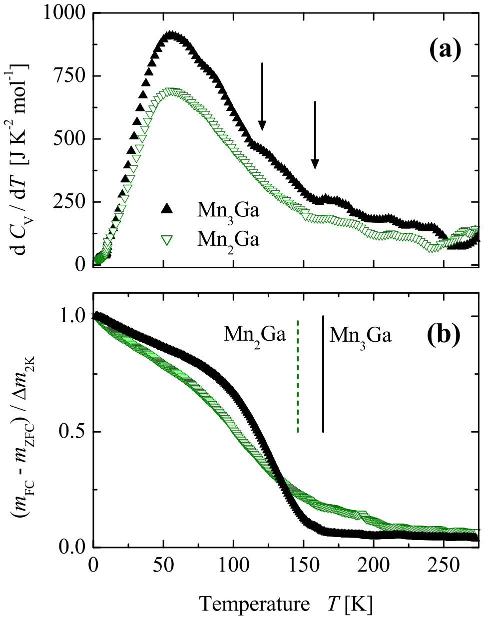

FIG. 15. (Color online) Low temperature magnetic anomaly of Mn_3Ga and Mn_2Ga. (a) shows the derivatives of the specific heats. (Changes in the slope of the Mn_3Ga curve are marked by arrows.) (b) shows the temperature dependence of the magnetic irreversibility. For better comparison, the differences are normalized to the value at 2 K. [The maxima of the $M(T)$ dependences in Fig. 12 are marked by vertical lines.]

it has been shown that the binary compounds $Mn_{3-x}Ga$, with x varying from 0 to 1.0, crystallize in the tetragonal DO_{22} phase with two inequivalent positions of the Mn atoms. The structural properties were determined by x-ray diffraction and extended x-ray absorption fine structure spectroscopy. Both the volume and the c/a ratio increase with increasing Mn content. From the electronic structure calculations, this can be attributed to a weakened hybridization between Ga and Mn states along the c axes in the compounds with lower Mn content. With increasing x, mainly—but not exclusively—the Mn_I atoms along the c axis are removed from the tetragonal unit cell. This model is supported by first-principles calculations that showed that the total magnetic moment should increase much stronger with x if only the Mn_I atoms are removed, while it should decrease if both types of Mn atoms are removed simultaneously. The result is an increase of the magnetic moment with x, because the Mn atoms at different crystallographic sites of the $Mn_{3-x}Ga$ compounds order ferrimagnetically. The experimentally observed change of the magnetic moment is also found in the *ab initio* calculations if more Mn_I atoms than Mn_{II} atoms are removed. The coercitivity and the different energy products of $Mn_{3-x}Ga$ decrease upon removal of Mn, allowing the magnetic properties and *hardness* to be tuned by varying the composition. The magnetization of the entire series vanishes at approximately 770 K. This is mainly caused by the structural transformation into the hexagonal DO_{19} phase. The entire series exhibits temperature dependent magnetic irreversibilities between zero-field-cooled and field-cooled conditions. A magnetic anomaly is found in all samples at temperatures between 145 and 172 K. This anomaly provides evidence that $Mn_{3-x}Ga$ is a series of magnetically frustrated ferrimagnets. The highest degree of frustration is found for the case of Mn_3Ga, where the magnetic anomaly is most pronounced.

ACKNOWLEDGMENTS

The authors thank the staff of the LNLS (Campinas) for support as well as Fabio Furlan Ferreira and Gustavo Azevedo (LNLS, Campinas) for help with the XRD and EXAFS measurements. The authors are very grateful to Hubert Ebert and Jan Minar (Munich) for developing and providing the SPRKKR computer code. Financial support by the DFG (Research Unit FOR559), the DAAD (D06/33952), and the CAPES PROBRAL (167/04) is gratefully acknowledged. The authors thank Martin Jourdan for providing the resistance measurements and Gerhard Jakob for helpful discussions (both at the Johannes Gutenberg-Universität, Mainz). Further support of this work was provided by the CNPq, the CT-Energ, and by the Brazilian Synchrotron Light Laboratory (LNLS) under proposals D04B-XAFS1-5711 and D10B-XPD-5708.

---

*felser@uni-mainz.de

[1] C. Pfleiderer, J. Boeuf, and H. v. Löhneysen, Phys. Rev. B **65**, 172404 (2002).

[2] C. Pfleiderer, Physica B **329**, 1085 (2003).

[3] S. Tomiyoshi, E. R. Cowley, and H. Onodera, Phys. Rev. B **73**, 024416 (2006).

[4] G. Kadar and E. Kren, Int. J. Magn. **1**, 143 (1971).

[5] S. Tomiyoshi, Y. Yamaguchi, and T. Nagamiya, J. Magn. Magn. Mater. **31**, 629 (1983).

[6] J. W. Cable, N. Wakabayashi, and P. Radhakrishna, Phys. Rev. B **48**, 6159 (1993).

[7] H. Takizawa, T. Yamashita, K. Uheda, and T. Endo, J. Phys.: Condens. Matter **14**, 11147 (2002).

[8] H. Ohmori, S. Tomiyoshi, H. Yamauchi, and H. Yamamoto, J. Magn. Magn. Mater. **70**, 249 (1987).

[9] J. W. Cable, N. Wakabayashi, and P. Radhakrishna, Solid State Commun. **88**, 161 (1993).

[10] T. Yamashita, H. Takizawa, T. Sasaki, K. Uheda, and T. Endo, J. Alloys Compd. **348**, 220 (2003).

[11] V. S. Goncharov and V. M. Ryzhkovskii, Inorg. Mater. **41**, 557 (2005).

[12] M. Ellner, J. Appl. Crystallogr. **13**, 99 (1980).

[13] A. Bekhti-Siad, A. Mokrani, C. Demangeat, and A. Khelil, J. Mol. Struct.: THEOCHEM **777**, 11 (2006).

[14] M. Suzuki, M. Shirai, and K. Motizuki, J. Phys.: Condens. Matter **4**, L33 (1992).

[15] V. M. Ryzhkovskii, V. P. Glazkov, V. S. Goncharov, D. P. Kozlenko, and B. N. Savenko, Phys. Solid State **44**, 2281 (2002).

[16] I. Tsuboya and M. Sugihara, J. Phys. Soc. Jpn. **18**, 143 (1963).

[17] M. Hasegawa and I. Tsuboya, J. Phys. Soc. Jpn. **20**, 464 (1965).

[18] H.-G. Meißner and K. Schubert, Z. Metallkd. **56**, 523 (1965).

[19] S. Wurmehl, H. C. Kandpal, G. H. Fecher, and C. Felser, J. Phys.: Condens. Matter **18**, 6171 (2006).

[20] E. Kren and G. Kadar, Solid State Commun. **8**, 1653 (1970).

[21] H. Niida, H. Hori, T. Onodera, Y. Yamaguchi, and Y. Nakagawa, J. Appl. Phys. **79**, 5946 (1996).

[22] J. Kübler, J. Phys.: Condens. Matter **18**, 9795 (2006).

[23] B. Balke, G. H. Fecher, J. Winterlik, and C. Felser, Appl. Phys. Lett. **90**, 152504 (2007).

[24] H. Ebert, in *Lecture Notes in Physics*, edited by H. Dreysse (Springer Verlag, Berlin, 1999), Vol. 535, pp. 191–246.

[25] H. Ebert, Munich SPRKKR, *Version 3.6*, 2005 (http://olymp.cup.uni-muenchen.de/ak/ebert/SPRKKR).

[26] S. H. Vosko and L. Wilk, Phys. Rev. B **22**, 3812 (1980).

[27] S. H. Vosko, L. Wilk, and M. Nusair, Can. J. Phys. **58**, 1200 (1980).

[28] J. P. Perdew, K. Burke, and M. Ernzerhof, Phys. Rev. Lett. **77**, 3865 (1996).

[29] H. C. N. Tolentino, A. Y. Ramos, M. C. M. Alves, R. A. Barrea, E. Tamura, J. C. Cezar, and N. Watanabe, J. Synchrotron Radiat. **8**, 1040 (2001).

[30] M. Newville, J. Synchrotron Radiat. **8**, 322 (2001).

[31] S. I. Zabinsky, J. J. Rehr, A. Ankudinov, R. C. Albers, and M. J. Eller, Phys. Rev. B **52**, 2995 (1995).

[32] H. C. Kandpal, G. H. Fecher, and C. Felser, J. Phys. D **40**, 1507 (2007).

[33] K. Binder and A. P. Young, Rev. Mod. Phys. **58**, 801 (1986).

[34] A. P. Ramirez, Annu. Rev. Mater. Sci. **24**, 453 (1994).

[35] I. Mirebeau, G. Iancu, M. Hennion, G. Gavoille, and J. Hubsch, Phys. Rev. B **54**, 15928 (1996).

[36] P. J. Ford, E. Babic, and J. A. Mydosh, J. Phys. F: Met. Phys. **3**, L75 (1973).

[37] I. A. Campbell, P. J. Ford, and A. Hamzic, Phys. Rev. B **26**, 5195 (1982).

[38] M. Escorne, A. Mauger, J. L. Tholence, and R. Triboulet, Phys. Rev. B **29**, 6306 (1984).